LETTER

Autophagosomes form at ER–mitochondria contact sites

Maho Hamasaki[1,2]*, Nobumichi Furuta[3]*, Atsushi Matsuda[4,5], Akiko Nezu[1,2], Akitsugu Yamamoto[6], Naonobu Fujita[1,2], Hiroko Oomori[7], Takeshi Noda[1,2], Tokuko Haraguchi[4,5], Yasushi Hiraoka[4,5], Atsuo Amano[3,8] & Tamotsu Yoshimori[1,2]

Autophagy is a tightly regulated intracellular bulk degradation/recycling system that has fundamental roles in cellular homeostasis[1]. Autophagy is initiated by isolation membranes, which form and elongate as they engulf portions of the cytoplasm and organelles. Eventually isolation membranes close to form double membrane-bound autophagosomes and fuse with lysosomes to degrade their contents. The physiological role of autophagy has been determined since its discovery, but the origin of autophagosomal membranes has remained unclear. At present, there is much controversy about the organelle from which the membranes originate—the endoplasmic reticulum (ER), mitochondria and plasma membrane[1,2]. Here we show that autophagosomes form at the ER–mitochondria contact site in mammalian cells. Imaging data reveal that the pre-autophagosome/autophagosome marker ATG14 (also known as ATG14L) relocalizes to the ER–mitochondria contact site after starvation, and the autophagosome-formation marker ATG5 also localizes at the site until formation is complete. Subcellular fractionation showed that ATG14 co-fractionates in the mitochondria-associated ER membrane[3–5] fraction under starvation conditions. Disruption of the ER–mitochondria contact site prevents the formation of ATG14 puncta. The ER-resident SNARE protein syntaxin 17 (STX17) binds ATG14 and recruits it to the ER–mitochondria contact site. These results provide new insight into organelle biogenesis by demonstrating that the ER–mitochondria contact site is important in autophagosome formation.

ATG14 is a unique subunit of the autophagy-specific phosphatidylinositol-3-OH kinase (PI(3)K) complex involved in autophagosome formation[6,7]. The ATG14 complex localizes to the isolation membrane, the cytoplasm and the ER. The anchoring of ATG14 to the ER is essential for autophagosome formation: under fed conditions, the ATG14 complex seems to diffuse within the ER membrane; after induction of autophagy by starvation, the complex assembles at several specific points before autophagosome formation[7]. Three-dimensional electron tomographic studies have shown that the isolation membrane is 'sandwiched' between two ER cisternae, one of which is connected to the isolation membrane by a narrow extension[8,9]. Taken together with a previous study showing that the ER-associated membrane known as the omegasome is the formation site[10], it is thought that the ER is the
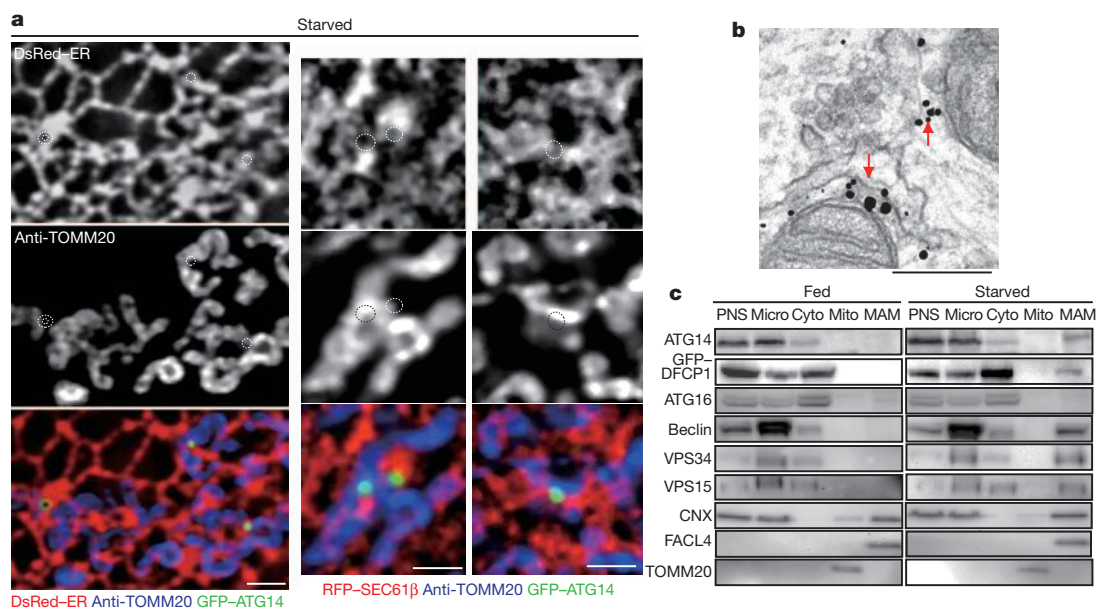

Figure 1 | ATG14 assembles at the ER–mitochondria contact site. a, COS7 cells co-transfected with GFP–ATG14 and DsRed–ER or RFP–SEC61β (an ER marker) were immunostained for the mitochondria marker TOMM20. Scale bars, 2 μm. **b**, An immunogold electron micrograph of starved HeLa cells expressing GFP–ATG14 probed with anti-GFP antibodies (red arrows). Scale bar, 200 nm. **c**, Immunoblots of subcellular fractions isolated from HEK293 cells stably expressing GFP–DFCP1. Cyto, cytosol; micro, microsome; mito, mitochondria; PNS, post-nuclear supernatant.

[1]Department of Genetics, Graduate School of Medicine, Osaka University, 2-2 Yamadaoka, Suita, Osaka 565-0871, Japan. [2]Laboratory of Intracellular Membrane Dynamics, Graduate School of Frontier Biosciences, Osaka University, 2-2 Yamadaoka, Suita, Osaka 565-0871, Japan. [3]Department of Oral Frontier Biology, Center for Oral Frontier Science, Osaka University Graduate School of Dentistry, 1-8 Yamadaoka, Suita, Osaka 565-0871, Japan. [4]National Institute of Information and Communications Technology, 588-2 Iwaoka, Iwaoka-cho, Nishi-ku, Kobe 651-2492, Japan. [5]Nuclear Dynamics Group, Graduate School of Frontier Biosciences, Osaka University, 1-3 Yamadaoka, Suita, Osaka 565-0871, Japan. [6]Department of Cell Biology, Faculty of Bio-Science, Nagahama Institute of Bio-Science and Technology, 1266 Tamura-cho, Nagahama, Shiga 526-0829, Japan. [7]Research Institute for Microbial Diseases, Osaka University, 3-1 Yamadaoka, Suita, Osaka 565-0871, Japan. [8]Department of Preventive Dentistry, Osaka University Graduate School of Dentistry, 1-8 Yamadaoka, Suita, Osaka 565-0871, Japan.
*These authors contributed equally to this work.

Table 1 | Quantification of GFP–ATG14 localization

Localization of ATG14 dots	$n = 380$
Adjacent to or on both ER and mitochondria	201 (52.9%)
Adjacent to or on ER only	177 (46.5%)
Adjacent to or on mitochondria only	1 (0.3%)
On neither organelle	1 (0.3%)

n denotes the number of ATG14 dots (described in Fig. 1a).

primary platform for autophagosome formation. Because the ER and mitochondria contact each other, we examine the relationship between autophagosome formation sites and the ER–mitochondria contact sites by triple-colour imaging. We show that ATG14 assembled exclusively at the ER–mitochondria contact site under starvation conditions (Fig. 1a, Table 1 and Supplementary Fig. 2a). Using immunoelectron microscopy, we observed that green fluorescent protein (GFP)-tagged ATG14 accumulated at ER–mitochondria contact sites under starved conditions (Fig. 1b and Supplementary Fig. 3a, b), and confirmed these observations in cells expressing Myc–ATG14 (Supplementary Fig. 3c, d). Our results support the idea that autophagosome formation takes place at the ER–mitochondria contact site during starvation.

We recovered the mitochondria-associated ER membrane (MAM)[3], which includes the contact sites, by Percoll centrifugation, identifying fractions using two MAM markers, the Ca^{2+}-binding chaperone calnexin (CNX) and fatty acid CoA ligase 4 (FACL4), as well as mitochondrial translocase of outer mitochondrial membrane 20 (TOMM20)[11–13]. Under fed conditions, endogenous ATG14 was not present in the MAM fractions (Fig. 1c); under starved conditions, however, the localization of ATG14 shifted markedly to the MAM. The localization of other components of the PI(3)K complex shifted in a similar manner to that of ATG14 (Fig. 1c). After starvation, double FYVE domain-containing protein 1 (DFCP1) translocated to the omegasome, which serves as a platform for autophagosome formation[10]. GFP–DFCP1 also shifted to the MAM under starved conditions (Fig. 1c). These results suggest that the ATG14 complex, as well as DFCP1, relocalizes to the MAM fractions during starvation.

An additional marker, ATG5, was used to observe autophagosome formation. ATG5 binds only to the isolation membrane (which eventually becomes an autophagosome) and detaches from the membrane after autophagosome formation completion[14]; it is thus an ideal and specific marker for the initial stages of autophagosome formation. Like ATG14, we found that 52.8% of ATG5 dots were observed at the ER–mitochondria contact site (Fig. 2a and Supplementary Fig. 2b, c).

Live-cell imaging was performed with three cameras to observe three markers simultaneously. Despite the fact that ATG5 is not an ER-resident protein, 98% of ATG5 dots were found on the ER after starvation (Fig. 2c). In fact, during the entire autophagosome formation process, most ATG5 dots never separated from the ER–mitochondria contact site (Fig. 2b, Supplementary Fig. 4 and Supplementary Videos 1–3). According to the live-cell imaging analysis, 98% of ATG5 dots localized on the ER and 79% were within 0.88 μm of the mitochondria (Fig. 2c, d). Localization near both organelles remained throughout the autophagosome formation process (Fig. 2e, f). However, unlike the stable association with the ER, association with mitochondria dynamically oscillated (but remained within 0.5 μm), which may explain why only 50% of ATG5 dots were observed on mitochondria of fixed cells. These observations show that the ER is the platform of autophagosome formation, and dynamic mitochondria association may have a role in providing components required for this process.

When the mitochondrial protein voltage-dependent anion channel 1 (VDAC1)[15] was overexpressed, it localized at ER–mitochondria contact sites, indicating its viability as an ER–mitochondria contact-site marker (Supplementary Fig. 5a). In live-cell imaging, GFP–ATG5 dots often appeared next to mCherry–VDAC1 dots and subsequently disappeared with time, whereas mCherry–VDAC1 dots remained, indicating the release of ATG5 from the ER–mitochondria contact site after completion of the autophagosome formation (Supplementary Fig. 5b and Supplementary Video 4). These results strongly suggest that autophagosome formation takes place at the ER–mitochondria contact site.

Phosphofurin acidic cluster sorting protein-2 (PACS-2), a cytosolic-sorting protein, has been implicated in the formation of ER–mitochondria contacts, and its knockdown uncouples mitochondria from the ER[12]. Puncta structures of GFP–ATG14 were barely visible in cells transfected with *PACS2* short interfering RNA (siRNA), a similar result to the phenotype of cells deficient in mitofusin 2 (MFN2), which tethers the ER to mitochondria[16,17] (Supplementary Fig. 6a). In starved PACS-2 knockdown and MFN2 knockdown cells, puncta structures of GFP–LC3, which represent the isolation membrane/autophagosome/autolysosome[18], were attenuated (Supplementary Fig. 6b). Indeed, the knockdown of PACS-2 caused a decrease in the lipidated form of LC3-II, which binds to autophagic membranes, and inhibited its degradation by autophagy (Supplementary Fig. 6c, d). Furthermore, siRNA knockdown of PACS-2 significantly decreased the levels of FACL4, ATG14 and GFP–DFCP1 in the MAM fraction, whereas only negligible changes were observed in other fractions (Supplementary
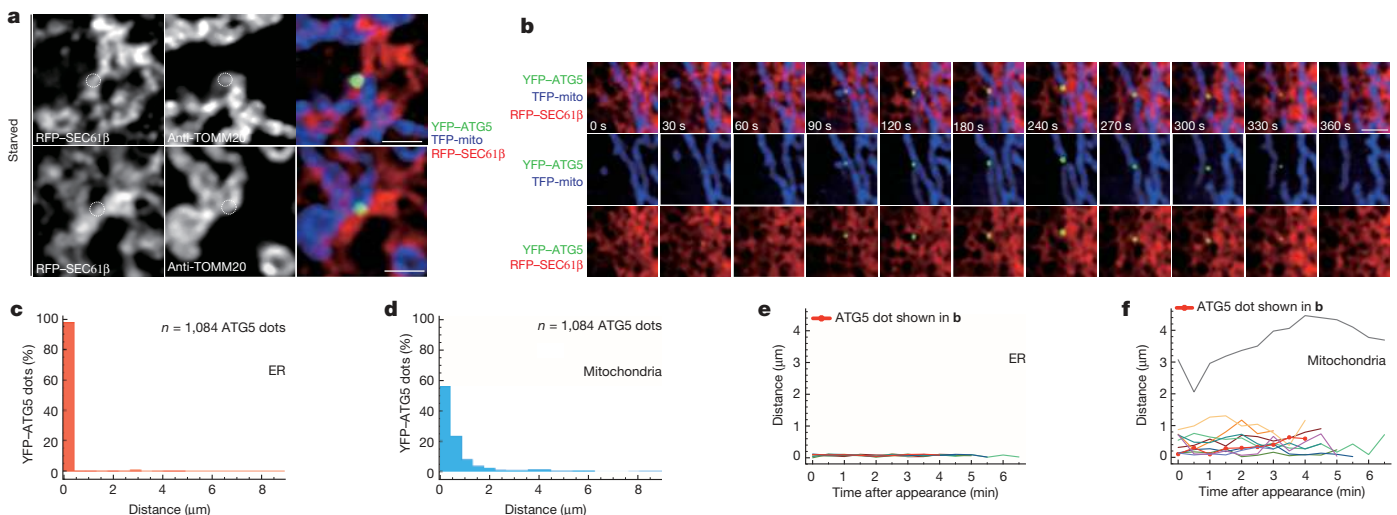
Figure 2 | Isolation membrane forms at ER–mitochondria contact sites.
a, COS7 cells stably expressing yellow fluorescent protein (YFP)–ATG5 were transfected with RFP–SEC61β and teal fluorescent protein (TFP)-mito, and immunostained for TOMM20. **b**, Time-lapse images of COS7 cells transfected with YFP–ATG5, RFP–SEC61β and TFP-mito under starved conditions. **c**, **d**, Distribution of distances of YFP–ATG5 dots from the centre to the surface of the ER (**c**) and to the surface of mitochondria (**d**). **e**, **f**, Distances of YFP–ATG5 dots over their lifetime for data from **c** (**e**) and **d** (**f**), respectively. All scale bars, 2 μm.
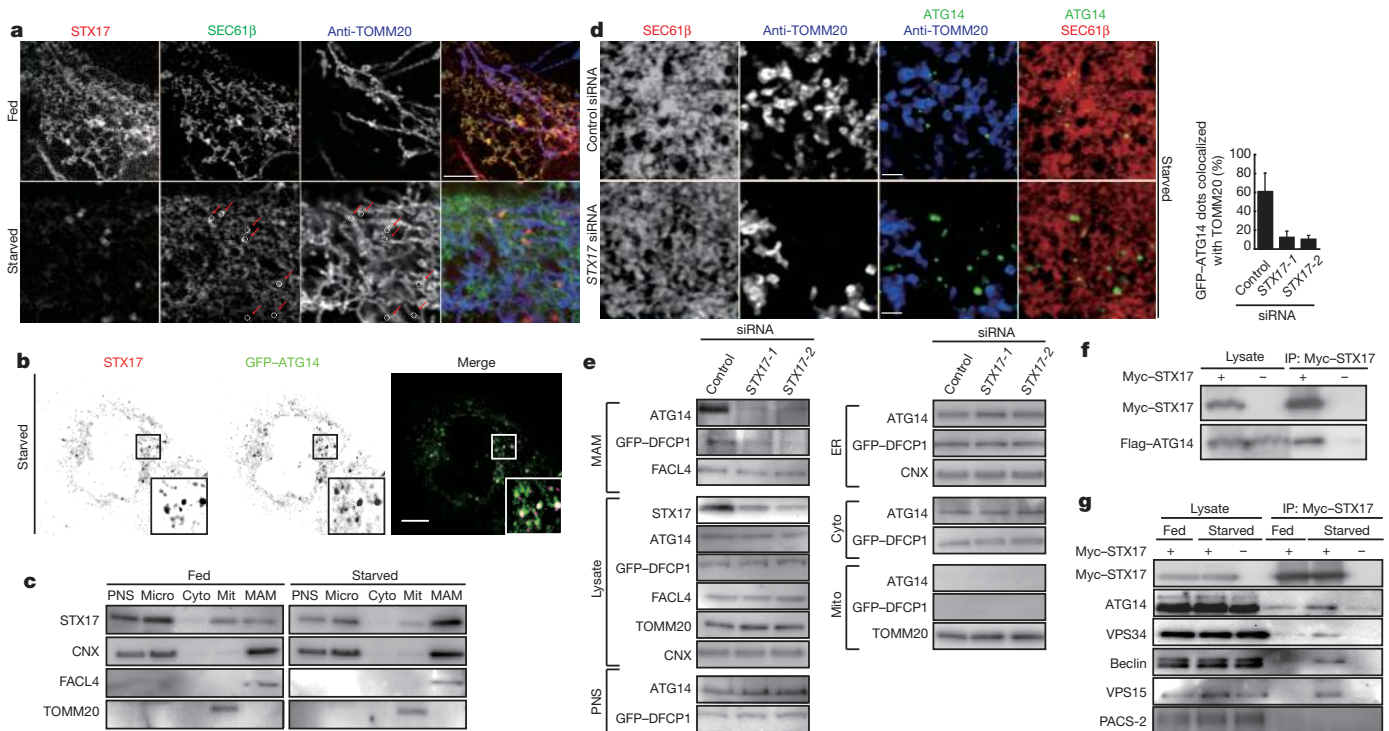
Figure 3 | STX17 regulates the relocalization of ATG14 to MAM. a, COS7 cells expressing GFP–SEC61β and STX17 were immunostained for TOMM20. **b**, HeLa cells expressing GFP–ATG14 were immunostained for STX17. **c**, Immunoblot of subcellular fractions of HEK293 cells. **d**, STX17 knockdown COS7 cells expressing GFP–ATG14 and RFP–SEC61β were immunostained for TOMM20. Error bars denote s.d. **e**, Immuoblot of subcellular fractions of STX17 knockdown (using two *STX17* siRNAs, *STX17-1* and *STX17-2*) HEK293 cells expressing GFP–DFCP1. **f**, Co-immunoprecipitation of STX17 and ATG14 using HeLa cells expressing Flag–ATG14 and Myc–STX17. **g**, Pull-down of ATG14 complex from HeLa cells expressing Myc–STX17 or Myc. Scale bars, 5 μm (**a**, **b**) and 2 μm (**d**).

Fig. 6e). These findings were also observed in MFN2 knockdown cells (Supplementary Fig. 6f), and suggest that the inhibition of the relocalization of ATG14 and DFCP1 to the ER–mitochondria contact site prevents the initiation of autophagosome formation.

Along with ATG14 and DFCP1, another ER protein, STX17, was seen to relocate to the ER–mitochondria contact sites after starvation (Fig. 3a). We identified STX17 in a screen for ER-resident SNARE proteins involved in autophagy against invading group A *Streptococcus* (GAS)[19,20] (Supplementary Fig. 7). STX17 is known to be a Qa-SNARE protein (a subfamily of Q (glutamate-containing)-SNARE proteins that occupy the same position as STX1A in the SNARE complex), but its function is not known[21]. STX17 dots at ER–mitochondria contact sites were extensively colocalized with ATG14 under starvation conditions (Fig. 3b). Furthermore, STX17 was abundant in microsome fractions under fed conditions, whereas it was mostly enriched in the MAM fraction of starved cells (Fig. 3c). Neither PACS-2 knockdown nor MFN2 knockdown had an effect on STX17 expression, but depletion of both inhibited the relocation of STX17 to the MAM fraction (Supplementary Fig. 6e, f).

GFP–ATG14 dots did not locate at the ER–mitochondria contact site in STX17 knockdown cells under starved conditions, although they did colocalize with other part of the ER (Fig. 3d). Consistently, ATG14 and GFP–DFCP1 were clearly decreased in the MAM fraction (Fig. 3e). By contrast, ATG14 depletion exhibited no effect on starvation-induced relocation of STX17 to the ER–mitochondria contact site (Supplementary Fig. 8). These data indicate that STX17 acts upstream of ATG14, and is responsible for directing ATG14 to the ER–mitochondria contact site. Given the functional relationship between STX17 and ATG14, we performed co-immunoprecipitation experiments. Myc–STX17 did not significantly co-immunoprecipitate with GFP–DFCP1 under starved conditions, whereas it did pull down Flag–ATG14 (Fig. 3f and data not shown). Similarly, endogenous ATG14 as well as other components of the complex clearly

co-immunoprecipitated with Myc–STX17 under starved conditions, whereas ATG14 barely precipitated in the absence of Myc–STX17 (Fig. 3g). These results suggest that Myc–STX17 associates with ATG14 only after starvation.

Whereas STX17 knockdown hinders the recruitment of ATG14 to the ER–mitochondria contact site, ATG14 was still able to assemble at other locations (Fig. 3d), indicating that STX17 is necessary for the recruitment of ATG14 to the ER–mitochondria contact site but not for the assembly of ATG14 dots. LC3-positive puncta were formed and accumulated in STX17 knockdown cells, indicating that the autophagosome maturation step was arrested (Supplementary Fig. 10b). We examined LC3 puncta by correlative light and electron microscopy in STX17 knockdown cells infected by GAS, and found that LC3-positive puncta represent isolation membranes (Fig. 4a and Supplementary Fig. 9). Immunogold electron microscopy of GFP–LC3, as well as conventional electron microscopy, showed accumulation of isolation membranes in STX17 knockdown cell under starvation conditions (Fig. 4b, c). In control cells, autolysosomes (autophagosomes fused with lysosomes) but few isolation membranes were observed; by contrast, in STX17 knockdown cells, isolation membranes were dominant whereas autolysosomes were nearly absent (Fig. 4c). Together, these data suggested that STX17 knockdown leads to an accumulation of isolation membranes deficient in autophagosome maturation. In addition, GFP–ATG5 dots accumulated to a considerable degree in these cells even under fed conditions, similar to the phenotype of inhibited autophagosome completion in ATG4B mutants[22] (Fig. 4d, e). Consistent with this, knockdown of STX17 significantly decreased autophagy, as detected by several assays: (1) degradation of p62 (also known as SQSTM1)[23] (Fig. 4f); (2) degradation of long-lived proteins[22], the clearance of which depends on autophagy (Fig. 4g); (3) autophagic flux as measured by the amount of LC3 in the presence or absence of lysosomal protease inhibitors[24] (Supplementary Fig. 10a); (4) fusion between autophagosomes and lysosomes, as measured by
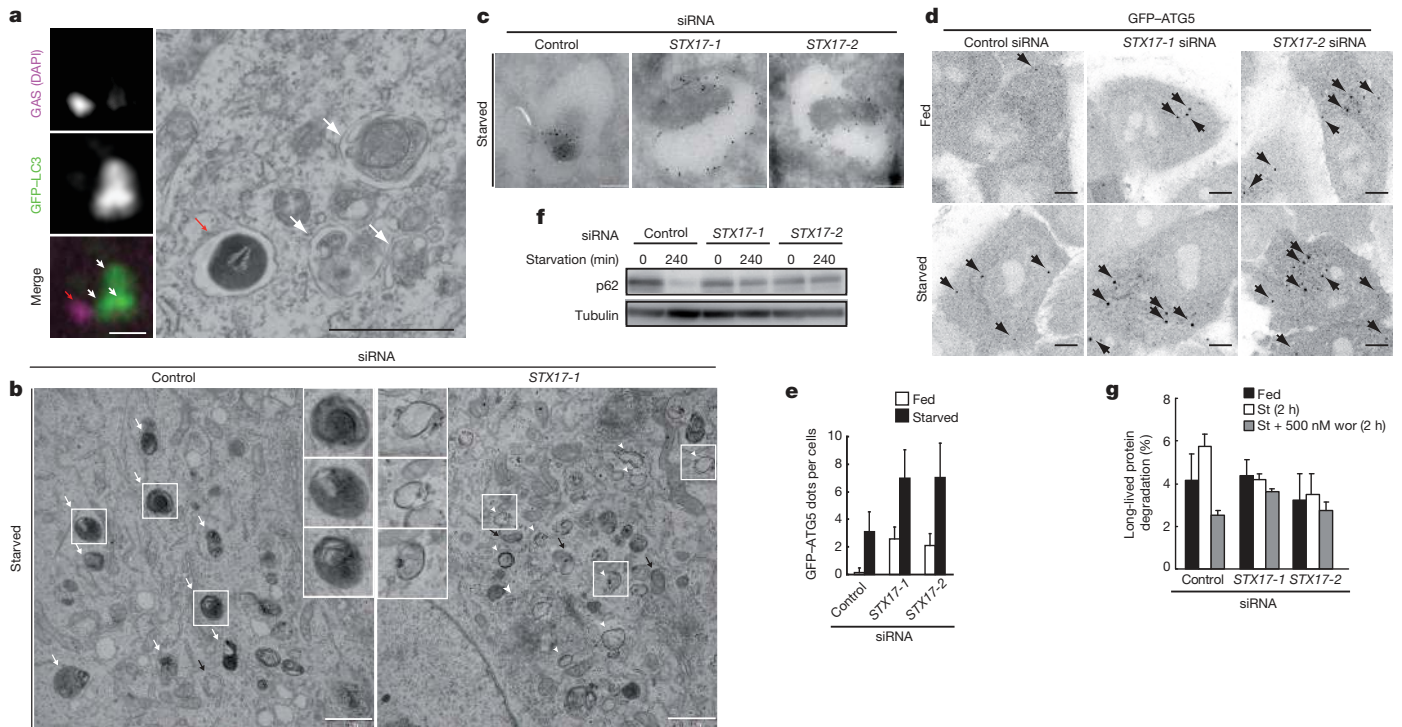
Figure 4 | Functional autophagosomes do not form in STX17 knockdown cells. a, Correlative light and electron microscopy analysis of STX17 knockdown HeLa cells expressing GFP–LC3 (white arrows) infected with GAS (red arrows). DAPI, 4′,6-diamidino-2-phenylindole. **b**, Electron micrographs of STX17 knockdown cells. White arrows denote autolysosomes, black arrows denote autophagosome, white arrowheads mark isolation membranes. **c**, Immunogold electron micrographs of STX17 knockdown HeLa cells stained for GFP–LC3. **d**, GFP–ATG5 dots (arrows) in STX17 knockdown HeLa cells. **e**, Quantification of staining in **d**. **f**, Immunoblot of p62 in STX17 knockdown cells. Tubulin was used as a loading control. **g**, Degradation of long-lived proteins in STX17 knockdown cells. St, starved; wor, wortmannin. All error bars denote s.d. Scale bars, 1 μm (**a**, **b**), 200 nm (**c**) and 5 μm (**d**).

monomeric red fluorescent protein (mRFP)–GFP tandem-tagged LC3 (ref. 25) (Supplementary Fig. 10b); (5) formation of large auto-phagosomes engulfing GAS (Supplementary Fig. 9); and (6) autophagic killing of GAS (Supplementary Fig. 7c). These results indicate that knockdown of STX17 blocks the completion of the autophagosome formation. Therefore, it is likely that STX17-dependent recruitment of ATG14 to the MAM is essential for the formation of functional autophagosomes. Our most plausible explanation for the phenotypic differences between knockdown of STX17 and knockdown of PACS-2 or MFN2 is the existence of STX17. In PACS-2 or MFN2 knockdown cells, the disruption of the MAM allows STX17 to interact with ATG14 (Supplementary Fig. 6g), blocking ATG14 dot formation. In STX17 knockdown cells, the absence of STX17 frees ATG14 to initiate isolation membrane formation.

Our findings provide new insights into two competing models for autophagosome biogenesis, that is, origin in the ER[7–9] or the mitochondria[16]. Results that have exclusively supported either model can now be explained by a new model in which the autophagosome is formed at the ER–mitochondria contact site (Supplementary Fig. 1). In retrospect, it seems that research groups arguing in favour of either single organelle model have been observing the same phenomenon from different sides. Our model does not exclude a possibility that formation independent on the contact site could still occur. We have also discovered a novel role for the ER–mitochondria contact site, a special crossing-over point between two organelles that is involved in a range of physiological functions. Many questions still remain, but these findings open new avenues for further study of the molecular mechanisms of autophagy.

METHODS SUMMARY

All cell lines were cultured in DMEM (Wako) supplemented with 10% heat-inactivated FBS (Invitrogen). siRNA and siRNA negative control (Stealth RNAi) were purchased from Invitrogen. Cells were examined under a fluorescence laser scanning confocal microscope (LSM510; Carl Zeiss and FV1000; Olympus) using the Zeiss LSM Image Browser software (Carl Zeiss) and FLUOVIEW (Olympus). Live-cell imaging was performed with the Yokogawa spinning disc confocal system (CSU-X1; Olympus). Immunoblotting[22], isolation of the MAM[3], conventional electron microscopy[22], immunoelectron microscopy[26], and the bulk protein degradation assay[22] were performed as described previously. All data are presented as mean ± s.d.

Full Methods and any associated references are available in the online version of the paper.

1. Mizushima, N., Yoshimori, T. & Ohsumi, Y. The role of Atg proteins in autophagosome formation. *Annu. Rev. Cell Dev. Biol.* **27,** 107–132 (2011).
2. Tooze, S. A. & Yoshimori, T. The origin of the autophagosomal membrane. *Nature Cell Biol.* **12,** 831–835 (2010).
3. Vance, J. E. Phospholipid synthesis in a membrane fraction associated with mitochondria. *J. Biol. Chem.* **265,** 7248–7256 (1990).
4. Rizzuto, R. *et al.* Close contacts with the endoplasmic reticulum as determinants of mitochondrial Ca²⁺ responses. *Science* **280,** 1763–1766 (1998).
5. Hayashi, T., Rizzuto, R., Hajnoczky, G. & Su, T.-P. MAM: more than just a housekeeper. *Trends Cell Biol.* **19,** 81–88 (2009).
6. Matsunaga, K. *et al.* Two Beclin 1-binding proteins, Atg14L and Rubicon, reciprocally regulate autophagy at different stages. *Nature Cell Biol.* **11,** 385–396 (2009).
7. Matsunaga, K. *et al.* Autophagy requires endoplasmic reticulum targeting of the PI3-kinase complex via Atg14L. *J. Cell Biol.* **190,** 511–521 (2010).
8. Hayashi-Nishino, M. *et al.* A subdomain of the endoplasmic reticulum forms a cradle for autophagosome formation. *Nature Cell Biol.* **11,** 1433–1437 (2009).
9. Ylä-Anttila, P., Vihinen, H., Jokitalo, E. & Eskelinen, E.-L. 3D tomography reveals connections between the phagophore and endoplasmic reticulum. *Autophagy* **5,** 1180–1185 (2009).
10. Axe, E. L. *et al.* Autophagosome formation from membrane compartments enriched in phosphatidylinositol 3-phosphate and dynamically connected to the endoplasmic reticulum. *J. Cell Biol.* **182,** 685–701 (2008).
11. Hayashi, T. & Su, T.-P. Sigma-1 receptor chaperones at the ER-mitochondrion interface regulate Ca²⁺ signaling and cell survival. *Cell* **131,** 596–610 (2007).
12. Simmen, T. *et al.* PACS-2 controls endoplasmic reticulum-mitochondria communication and Bid-mediated apoptosis. *EMBO J.* **24,** 717–729 (2005).
13. Künkele, K. P. *et al.* The preprotein translocation channel of the outer membrane of mitochondria. *Cell* **93,** 1009–1019 (1998).

14. Mizushima, N. *et al.* Dissection of autophagosome formation using Apg5-deficient mouse embryonic stem cells. *J. Cell Biol.* **152,** 657–668 (2001).
15. Szabadkai, G. *et al.* Chaperone-mediated coupling of endoplasmic reticulum and mitochondrial Ca²⁺ channels. *J. Cell Biol.* **175,** 901–911 (2006).
16. Hailey, D. W. *et al.* Mitochondria supply membranes for autophagosome biogenesis during starvation. *Cell* **141,** 656–667 (2010).
17. de Brito, O. M. & Scorrano, L. Mitofusin 2 tethers endoplasmic reticulum to mitochondria. *Nature* **456,** 605–610 (2008).
18. Kabeya, Y. *et al.* LC3, a mammalian homologue of yeast Apg8p, is localized in autophagosome membranes after processing. *EMBO J.* **19,** 5720–5728 (2000).
19. Furuta, N., Fujita, N., Noda, T., Yoshimori, T. & Amano, A. Combinational soluble *N*-ethylmaleimide-sensitive factor attachment protein receptor proteins VAMP8 and Vti1b mediate fusion of antimicrobial and canonical autophagosomes with lysosomes. *Mol. Biol. Cell* **21,** 1001–1010 (2010).
20. Steegmaier, M., Oorschot, V., Klumperman, J. & Scheller, R. H. Syntaxin 17 is abundant in steroidogenic cells and implicated in smooth endoplasmic reticulum membrane dynamics. *Mol. Biol. Cell* **11,** 2719–2731 (2000).
21. Fujita, N. *et al.* An Atg4B mutant hampers the lipidation of LC3 paralogues and causes defects in autophagosome closure. *Mol. Biol. Cell* **19,** 4651–4659 (2008).
22. Bjørkøy, G. *et al.* Monitoring autophagic degradation of p62/SQSTM1. *Methods Enzymol.* **452,** 181–197 (2009).
23. Mizushima, N. & Yoshimori, T. How to interpret LC3 immunoblotting. *Autophagy* **3,** 542–545 (2007).
24. Kimura, S., Noda, T. & Yoshimori, T. Dissection of the autophagosome maturation process by a novel reporter protein, tandem fluorescent-tagged LC3. *Autophagy* **3,** 452–460 (2007).
25. Yamamoto, A. & Masaki, R. Pre-embedding nanogold silver and gold intensification. *Methods Mol. Biol.* **657,** 225–235 (2010).
26. Kageyama, S. *et al.* The LC3 recruitment mechanism is separate from Atg9L1-dependent membrane formation in the autophagic response against Salmonella. *Mol. Biol. Cell* **22,** 2290–2300 (2011).

METHODS

Cell culture and transfection. All cell lines were cultured in DMEM (Wako) supplemented with 10% heat-inactivated FBS (Invitrogen). HeLa cells stably expressing enhanced GFP (eGFP)–LC3 and COS7 cells stably expressing YFP–ATG5 were constructed as previously described[14]. HeLa cells stably expressing eGFP–ATG5 were a gift from N. Fujita. Wild-type and ATG14-deficient mouse embryonic fibroblasts were constructed as previously described[26]. HEK293 cells stably expressing eGFP–DFCP1 were established as previously described[10]. LipofectAMINE2000 (Invitrogen) was used for transfection. For amino acid starvation, cells were cultured in EBSS (Sigma) without amino acids or FBS for 2 h. Stable transformants were selected in complete medium containing 500 μg ml^{-1} G418 (Sigma).

Antibodies and immunoblotting. Antibodies against the following proteins were mouse monoclonal: Myc (MBL), GFP (Abcam), tubulin (Sigma), PDI (Stressgen) and CNX (BD Bioscience). Rabbit polyclonals include: LC3 (MBL), TOMM20 (Abcam), FACL4 (Abcam), STX17 (Sigma), ATG14 (MBL), VPS34 (Cell Signaling), VPS15 (MBL), beclin (MBL), MFN2 (Sigma) and PACS-2 (ProteinTech Group). Alexa Fluor-conjugated secondary antibodies (goat anti-mouse IgG and goat anti-Rabbit IgG) used for fluorescence microscopy were purchased from Invitrogen. Immunoblotting was performed as previously described[27].

siRNAs and plasmids. siRNA duplexes targeting *STX17* (HSS123730 and HSS123732), *STX18* (HSS122692 and HSS122693), *SEC20* (also known as *BNIP1*) (HSS141385 and HSS141386), *SEC22A* (HSS120253 and HSS120254), *SEC22C* (HSS145024 and HSS145025), *SLT1* (also known as *USE1*) (HSS125167 and HSS125168), *PACS2* (HSS146278 and HSS146279), *ATG14* (HSS117763 and HSS117764), *MFN2* (HSS115028 and HSS115029), and siRNA negative control (Stealth RNAi) were purchased from Invitrogen. siRNA for *VTI1B* was described previously[19].

Expression vectors for mCherry-C1 plasmids[5] and mRFP-GFP-LC3 (ref. 24) plasmids were constructed. GFP–ATG14 and Flag–ATG14 were also established[7]. mCherry- or GFP-Cyt b5-TM was constructed as described previously[28]. GFP–SEC61β was a gift from T. Rapoport. DsRed–ER was a gift from K. Tabata. DsRed2-mito was obtained from Clontech. TFP-mito was constructed by replacing DsRed using PCR fragments. To construct Myc–STX17 plasmids, complementary DNA cloned from genomic DNA of HeLa cells was inserted into pcDNA3.1/Myc-His(−)A (Invitrogen) using engineered EcoRI and XhoI sites. To construct Myc–STX17(ΔSNARE) plasmids, the STX17(ΔSNARE) domain was generated by PCR (primers: 5′-ATGTCTGAAGATGAAGAAAAAGTG-3′ and 5′-TTAAGCCTTCCCTAAGTTTTTGG-3′). The PCR fragment was digested with EcoRI and XhoI and used to replace the *STX17* cDNA in the Myc–STX17 plasmid. To construct Myc–ATG14 plasmids, cDNA from Flag–ATG14 was inserted into pcDNA3.1/Myc-His(−)A (Invitrogen) using engineered EcoRI and KpnI sites. To construct mCherry or GFP-VDAC1 plasmids, cDNA from genomic DNA of HeLa cells was inserted into mCherry-C1 or EGFP-C1 (Invitrogen) using engineered SalI and BamHI sites. To construct mCherry or GFP–DRP1 plasmids, cDNA from genomic DNA of HeLa cells was inserted into mCherry-C1 or EGFP-C1 (Invitrogen) using engineered SalI and BamHI sites. To construct an mCherry-LC3 plasmid, PCR was performed to generate mCherry cDNA with exogenous restriction sites for BamHI and NotI at the 5′ and 3′ ends, respectively. The PCR fragment obtained after digestion with each restriction enzyme was inserted into pMRX-mCherry. LC3 cDNA cloned from the genomic DNA of HeLa cells was inserted into pMRX-mCherry using engineered EcoRI and XhoI sites.

RT–PCR and real-time PCR. PCR with reverse transcription (RT–PCR) and real-time PCR were preformed as described previously[29]. The sequences of the oligonucleotides were as follows: *STX17* (forward, 5′-GCCGTCTTGAACCAGCT ATC-3′; reverse, 5′-TTCATGCAACTTGTCCCAGA-3′), *STX18* (forward, 5′-TCACATTGGCAAACTGAGAGAT-3′; reverse, 5′-TCTGGGCATCCTGGTC TATC-3′), *SEC20* (forward, 5′-ACGTCCGGATCTGTAACCAA-3′; reverse, 5′-AAGGGTCCTGAACAATCACG-3′), *SEC22A* (forward, 5′-ATGCTTTCGAG GAAACTTGC-3′; reverse, 5′-GAGAAGGCGAGAACATTTGG-3′), *SEC22C* (forward, 5′-GAGTTTAGCCTTGCGACTGG-3′; reverse, 5′-AGGAGCAGAT AGCCATGCAG-3′), *SLT1* (forward, 5′-GTCGAGGCTGGAGCTAAACC-3′; reverse, 5′-GGCCTGCAACATGTCCTCTA-3′), and *GAPDH* (forward, 5′-GTGGTCTCCTCTGACTTCAACAG-3′; reverse, 5′-CTGTAGCCAAATTCGT TGTCATAC-3′). The expression levels of messenger RNA are indicated as the relative cycle number for a given gene normalized against the cycle number for *GAPDH*. Each reaction was repeated at least three times to assess reproducibility.

Fluorescence microscopy. Fluorescence microscopy was performed as described previously[5]. To detect STX17, cells were permeabilized with 0.1% Triton X-100, and blocked with 1% normal goat serum (Abcam).

Proteinase inhibitor. E64d and pepstatin A were purchased from the Peptide Institute. Cells were transfected with siRNA against *STX17* or with control siRNA. After 48 h of incubation, the cells were cultured in EBSS containing E64d (10 μg ml^{-1}) and pepstatin A (30 μg ml^{-1}) or in a solution lacking inhibitors (control; dimethylsulphoxide 1.1 μg ml^{-1}) at the appropriate times. Lysates were examined by western blotting using antibodies against LC3 and tubulin.

GAS infection and bacterial viability assay. Infection with GAS (strain JRS4) and the colony-forming units (c.f.u.) viability assay were performed as described previously[30].

Immunoprecipitation analysis. Immunoprecipitation analysis was performed using the c-Myc-tagged protein mild purification kit (MBL). Twenty-million cells were suspended in lysis buffer (20 mM Tris-HCl, pH 7.5, 150 mM NaCl, 5 mM EDTA and 1% CHAPS). Cell lysates were centrifuged at 15,000g for 10 min. The resulting supernatant was transferred to a spin column and incubated with anti-c-Myc beads for 1 h at 4 °C. Anti-c-Myc beads in the spin column were incubated with elution peptide solution for 30 s on ice and centrifuged for 10 s.

Electron microscopy and bulk protein degradation assay. Conventional electron microscopy was performed as described previously[31]. Immunoelectron microscopy was performed using a rabbit polyclonal antibody against GFP (a gift from N. Nakamura) by applying the pre-embedding gold enhancement method as described previously[25]. Samples were analysed with an electron microscope (H7600; Hitachi). Correlative light and electron microscopy was performed as described previously[26], as was the long-lived proteins degradation assay[21]. In brief, degradation of long-lived proteins depends on the autophagic activity. Cells were seeded in 24-well dishes and incubated overnight. On the next day, the cells were exchanged into labelling medium containing ^{14}C-valine (1.5 Ci ml^{-1}) and again incubated overnight. Cells were exchanged into chase medium (DMEM supplemented with 10% FBS and 10 mM unlabelled valine) and further incubated for 4 h to remove the contribution of short-lived proteins. After the chase period, media was replaced with either growth medium containing 10 mM valine or EBSS containing 10 mM valine (to induce autophagy). After 2 h incubation, the media were collected, and the trichloroacetic acid (TCA)-soluble fraction was analysed by scintillation counting. The cells were lysed in ice-cold RIPA buffer (25 mM Tris-HCl, pH 7.5, 150 mM NaCl, 0.1% SDS, 1% Triton X-100, 1% deoxycholate, 5 mM EDTA and protease inhibitor cocktail (Roche)); the TCA-insoluble fraction was isolated and analysed by scintillation counting. To determine the rate of long-lived protein degradation, the count in the TCA-soluble fraction in the medium was divided by the total cellular count.

Tokuyasu sampling and immunolabelling. Cells transfected with Myc–ATG14 were pre-fixed for 10 min (4% paraformaldehyde/0.1% glutaraldehyde in PHEM (120 mM PIPES, 50 mM HEPES, 20 mM EGTA and 4 mM MgCl$_2$, pH 6.9)) then fixed with fresh 4% paraformaldehyde in PHEM for 30 min at room temperature. Cells were scraped, resuspended in 10% gelatin/PBS, pelleted by centrifugation, and immediately placed on ice until the gelatin solidified. Gelatin-embedded samples were infiltrated with 2.3 M sucrose (in 0.1 M phosphate buffer), placed at 4 °C overnight on a rotating wheel mounted onto sample pins, and frozen in liquid nitrogen. Subsequently, samples were cryo-sectioned at 60 nm thickness using an FC6/UC6 cryo-ultramicrotome (Leica), and selected with a 1:1 mixture of 2% methylcellulose (0.025 Pa s^{-1}; Sigma) and 2.3 M sucrose. After thawing, sections were first reacted with anti-Myc antibodies (MBL) diluted 1:100, then with rabbit anti-mouse antibodies (Invitrogen) diluted 1:1,000, and finally with 10-nm gold-conjugated protein A following an established protocol[32]. For double labelling, an anti-PDI antibody was used (Stressgen). Sections were embedded in 4% uranyl acetate/2% methylcellulose (ratio 1:9)[33] and viewed using a JEOL 1010 electron microscope.

Live-cell imaging. Live-cell imaging was performed at 37 °C using an Olympus IX81 microscope with a ×100 immersion objective lens (numerical aperture 1.40) equipped with a Yokogawa spinning disc confocal system (CSU-X1) and three EMCCD cameras (Andor iXon3). Images were acquired by Andor iQ live cell imaging software.

Image analysis. Images were digitally processed as follows for subsequent statistical analyses. Bleed-through of the CFP channel in the YFP channel was removed by spectral unmixing. The background fluorescence in the YFP channel was then normalized using time-averaged images. Next, all channels were processed by a denoising algorithm to improve the signal-to-noise ratio in the fluorescence images[34] and finally by constrained iterative deconvolution. The RFP channel is shown in logarithmic scale to visualize both the peripheral mesh structures and the thick network around the nucleus. The three-dimensional distance between the centre of a YFP–ATG5 dot and the surface of the ER/mitochondria was measured with custom-made software. The mitochondria and ER had relatively constant fluorescence intensities and thus adaptive thresholding was effective to distinguish their surfaces. On the other hand, because YFP–ATG5 dots have variable signal intensities, thresholding alone can change their size. Therefore, to reduce thresholding artefacts, centres rather than surface coordinates of the YFP–ATG5 dots were used. A surface of the ER/mitochondria complex was represented as the nearest pixel to the centre of a YFP–ATG5 dot.

27. Kamimoto, T. *et al.* Intracellular inclusions containing mutant α1-antitrypsin Z are propagated in the absence of autophagic activity. *J. Biol. Chem.* **281,** 4467–4476 (2006).
28. Saitoh, T. *et al.* Atg9a controls dsDNA-driven dynamic translocation of STING and the innate immune response. *Proc. Natl Acad. Sci. USA* **106,** 20842–20846 (2009).
29. Kawai, S., Yamauchi, M., Wakisaka, S., Ooshima, T. & Amano, A. Zinc-finger transcription factor odd-skipped related 2 is one of the regulators in osteoblast proliferation and bone formation. *J. Bone Miner. Res.* **22,** 1362–1372 (2007).
30. Nakagawa, I. *et al.* Autophagy defends cells against invading group A *Streptococcus. Science* **306,** 1037–1040 (2004).
31. Fujita, N. *et al.* The Atg16L complex specifies the site of LC3 lipidation for membrane biogenesis in autophagy. *Mol. Biol. Cell* **19,** 2092–2100 (2008).
32. Slot, J. W. & Geuze, H. J. Cryosectioning and immunolabeling. *Nature Protocols* **2,** 2480–2491 (2007).
33. Griffiths, G., McDowall, A., Back, R. & Dubochet, J. On the preparation of cryosections for immunocytochemistry. *J. Ultrastruct. Res.* **89,** 65–78 (1984).
34. Boulanger, J., Kervrann, C. & Bouthemy, P. A simulation and estimation framework for intracellular dynamics and trafficking in video-microscopy and fluorescence imagery. *Med. Image Anal.* **13,** 132–142 (2009).